

We will assume a typical photoionized temperature of 8000 K, so that $c_s \approx 10 \text{ km s}^{-1}$ and $M_0 = v_{10}$, yielding

$$\tau_{\text{gas}} = -\ln(1 - 8.42 \times 10^{-6} v_{10}^2 n^2 R_{0,\text{pc}}^3 S_{49}^{-1}), \quad (\text{B8})$$

where

$$R_{0,\text{pc}} = R_0 / (1 \text{ pc})$$

The dust opacity is approximately constant at FUV to EUV wavelengths, so the dust optical depth of the shocked shell to ionizing photons follows from equations (8) and (21) as $\tau_d = \frac{3}{8} \tau$.

The hydrogen ionization fraction, y , at the outer edge of the shocked shell then follows as

$$\frac{y^2}{1-y} = \frac{\sigma \mathcal{F}}{\alpha_B n} e^{-(\tau_d + \tau_{\text{gas}})}, \quad (\text{B9})$$

where σ is the effective hydrogen photoionization cross section, averaged over the local ionizing spectrum. Since the frequency-dependent cross section, $\sigma_\nu \sim \nu^{-3}$, is strongly peaked at the threshold, the local EUV spectrum becomes harder with increasing τ_{gas} , as the lower frequency photons are selectively absorbed,¹⁹ leading to a reduction in the effective σ . An approximate fit to the results in Appendix A of ? is

$$\sigma = 0.5 \sigma_0 e^{-\tau_{\text{gas}}/3} \quad (\text{B10})$$

where $\sigma_0 = 6 \times 10^{-18} \text{ cm}^2$ is the threshold cross-section. Although this was derived for a particular ionizing spectrum (40 000 K black body), we adopt it for all our hot stars.

This paper has been typeset from a $\text{\TeX}/\text{\LaTeX}$ file prepared by the author.

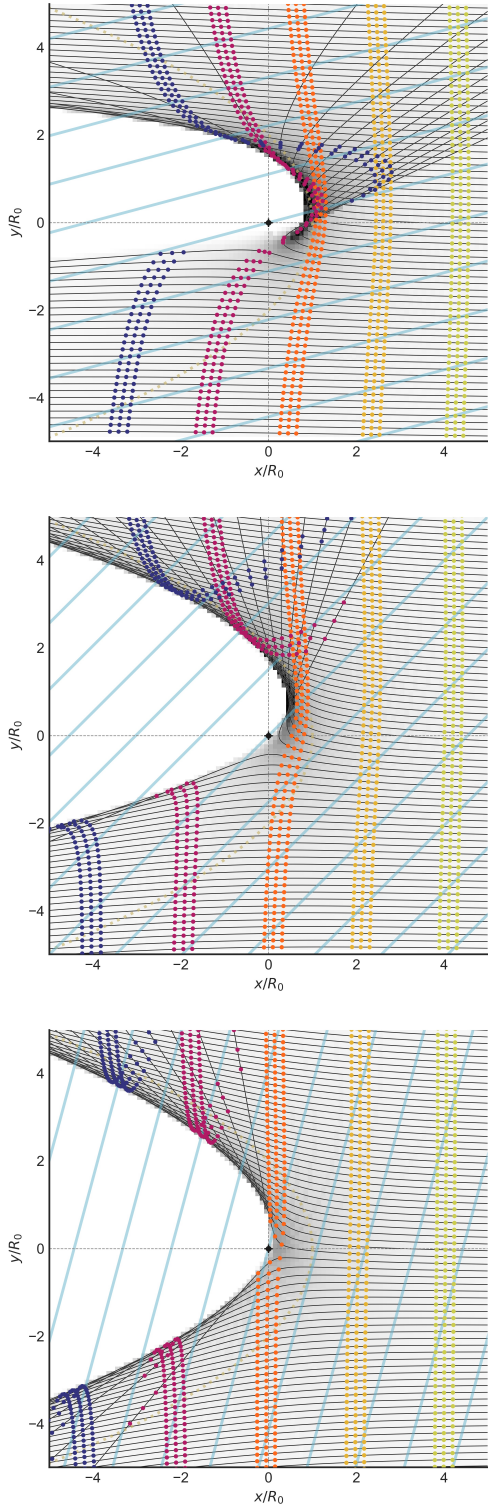


Figure 10. Grain trajectories for magnetised dust waves in the limit of no gas drag and small gyro-radius.

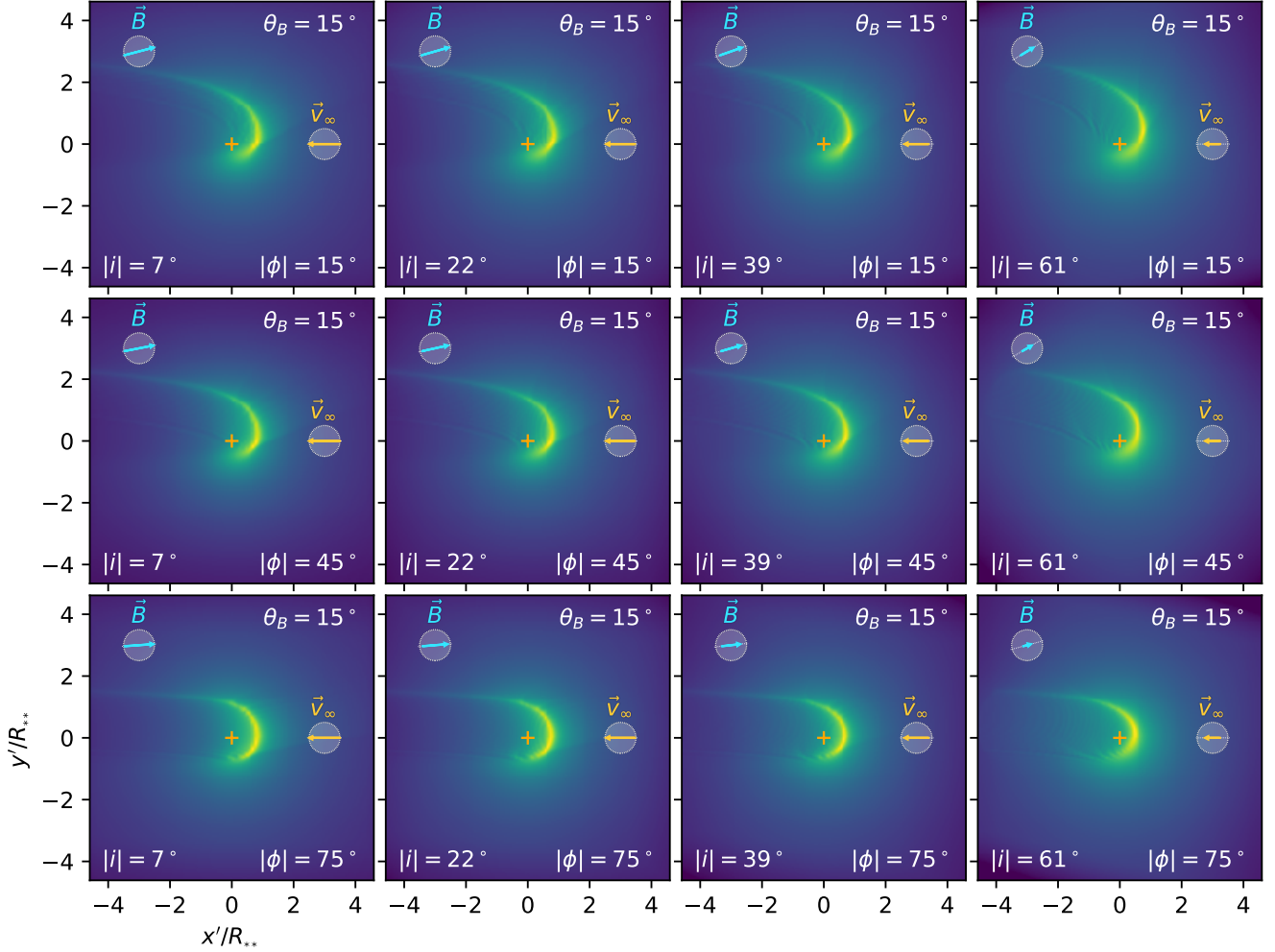
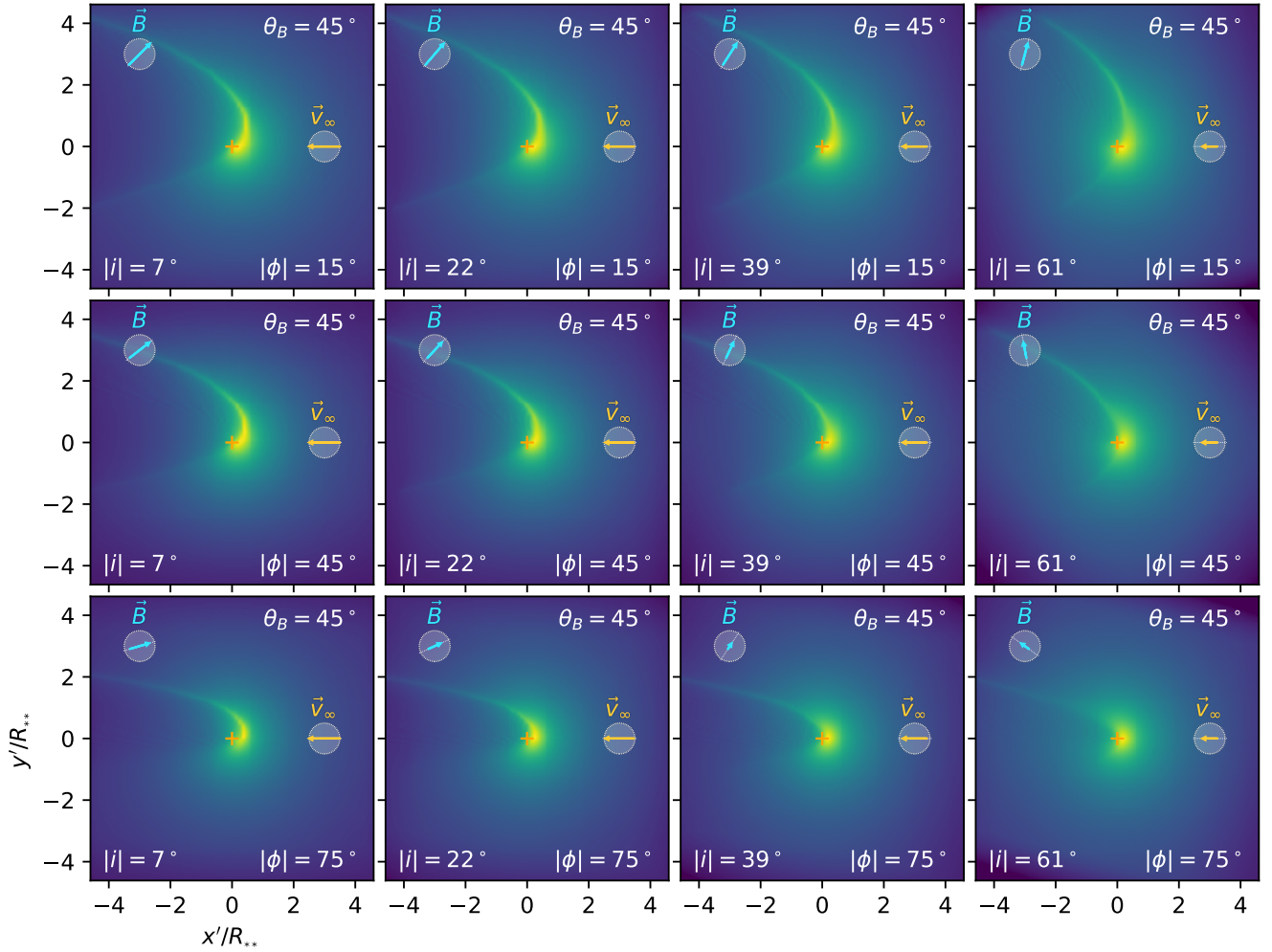


Figure 11. xxx

**Figure 12.** xxx

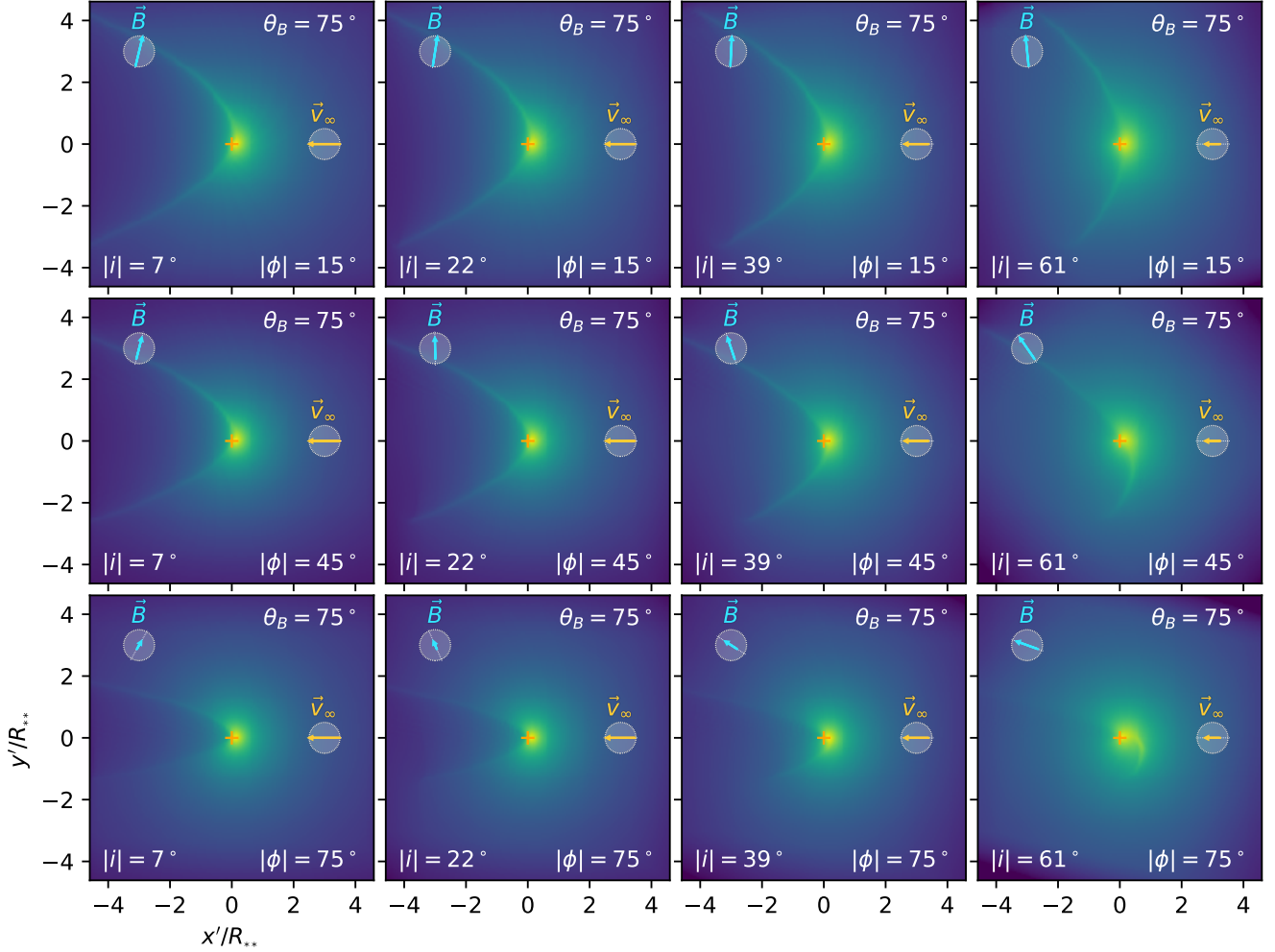


Figure 13. xxx

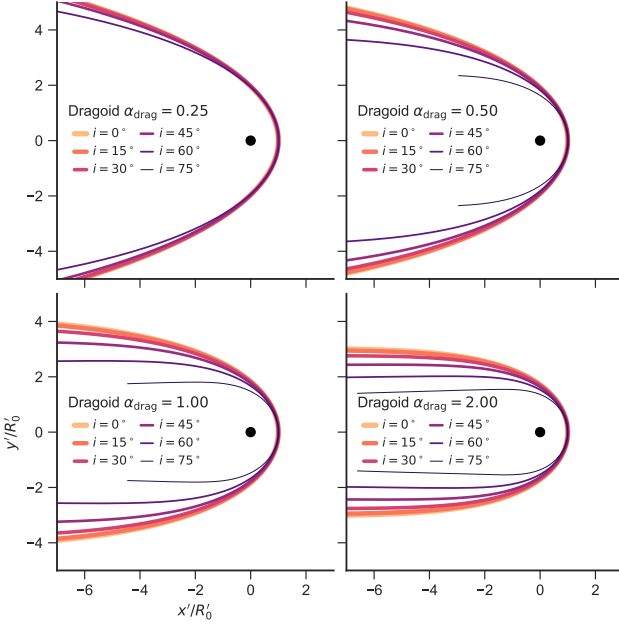


Figure 14. Apparent bow shapes in the plane of the sky for parallel-stream dragoids as a function of inclination angle. Drag coefficient, α_{drag} increases from top-left to bottom-right. Inclination $|i|$ is shown in 15° increments, indicated by line color and thickness (see key).

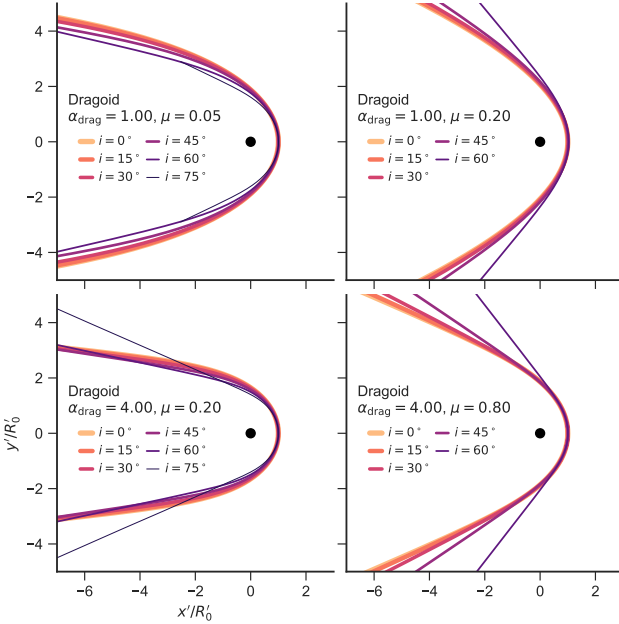


Figure 15. As Fig. 14 but for divergent stream dragoids. Drag coefficient increases from top to bottom, while degree of divergence increases from left to right.

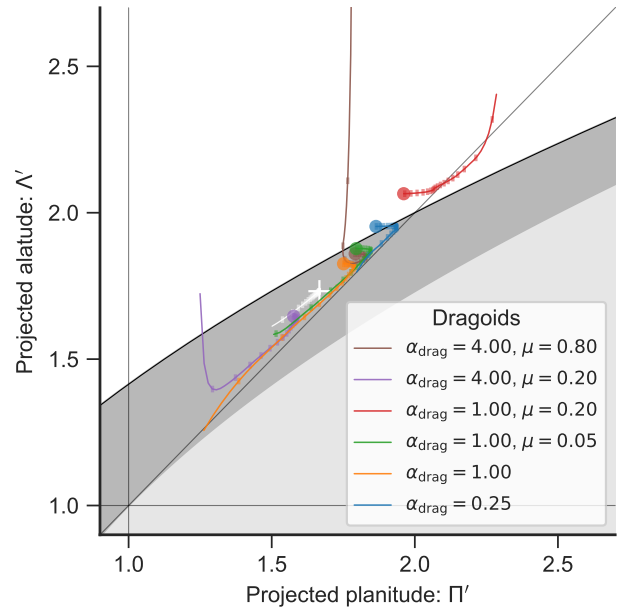


Figure 16. Apparent projected shapes of dragoids in the Π' – Λ' plane. Colored symbols indicate the $|i| = 0$ position for selected models (see key). Thin lines show the inclination-dependent tracks of each model, with tick marks along each track for 20 equal-spaced values of $|\sin i|$. Gray shaded regions are as in Fig. 11a of ?. The wilkinoid track is shown in white.

[t!]

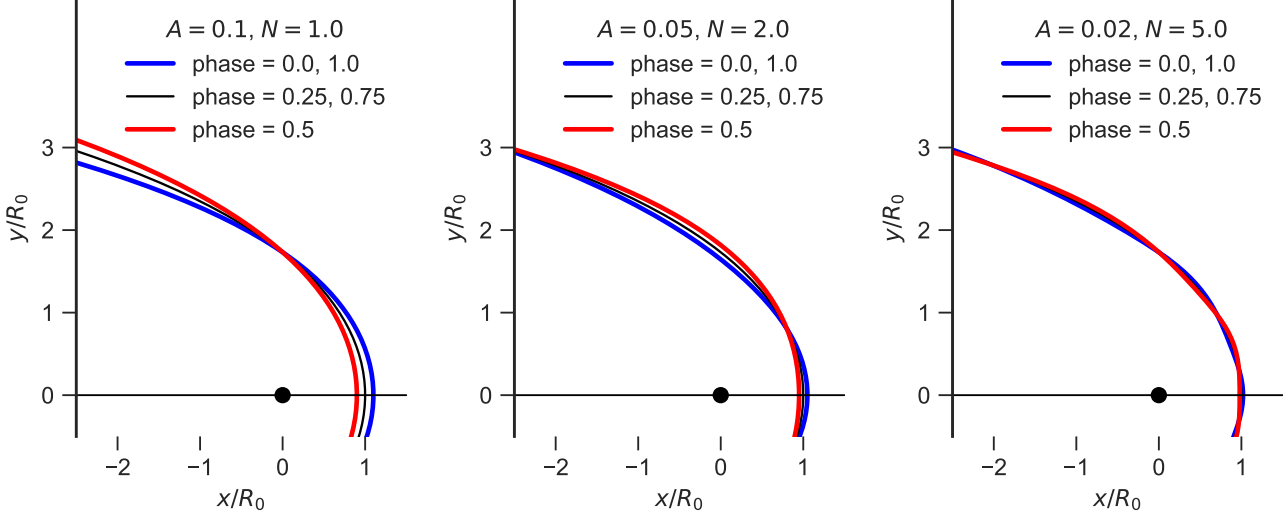


Figure 17. Small-amplitude standing wave perturbations to wilkinoid bow shapes. The maximum deviations from the base shape are seen at phases $\phi = 0$ (blue line) and $\phi = 0.5$ (red line), while the perturbation is zero at $\phi = 0.25$ and 0.75 (black line). Results are shown left to right for increasing wave numbers N and decreasing amplitudes A : (a) $A = 0.1$, $N = 1.0$, (b) $A = 0.05$, $N = 2.0$, (c) $A = 0.02$, $N = 5.0$.

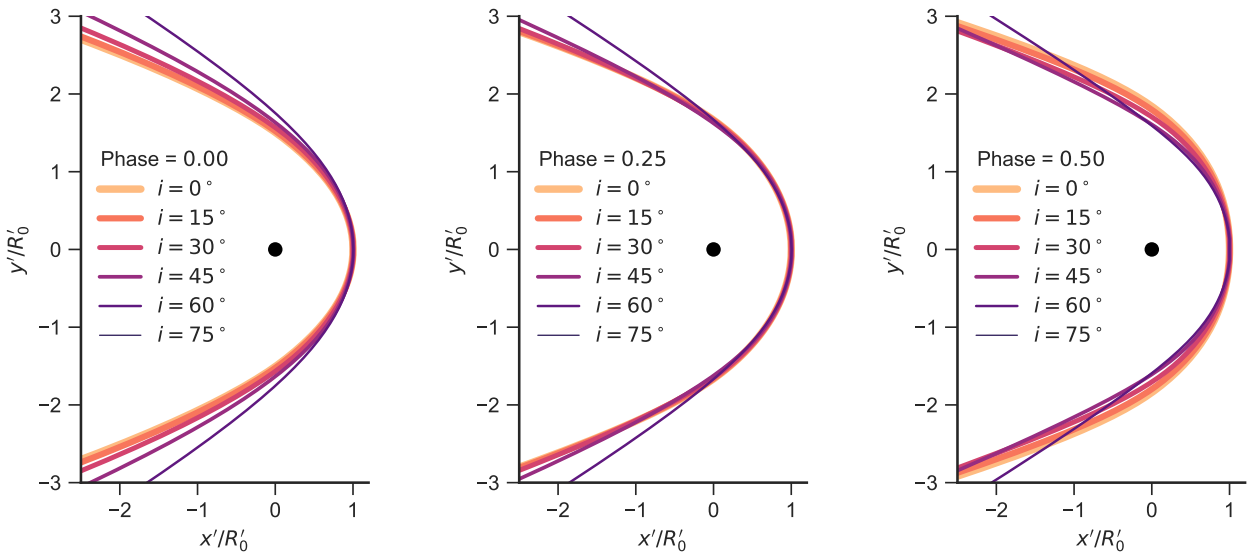
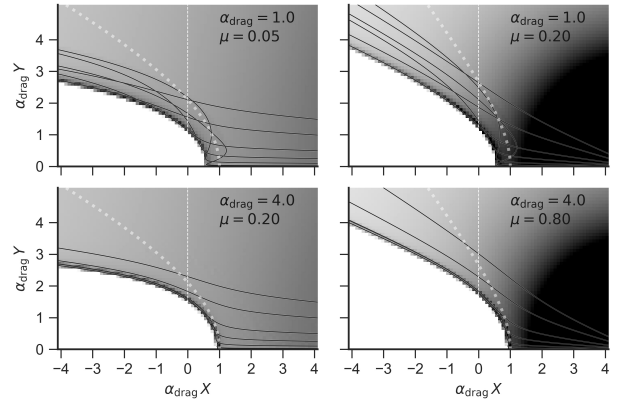
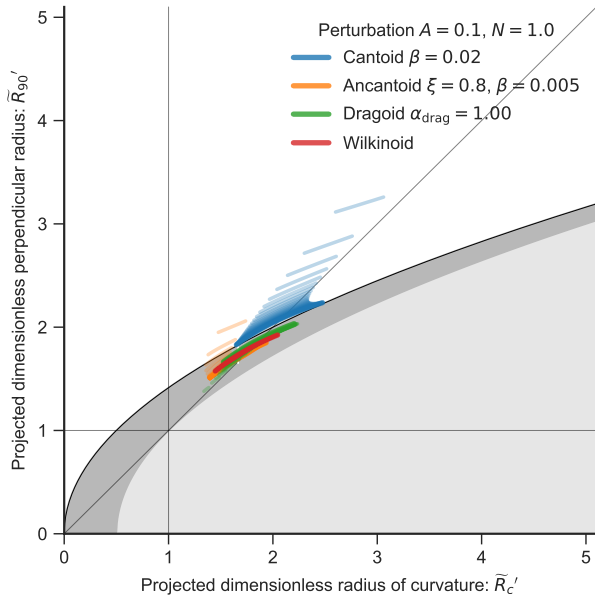
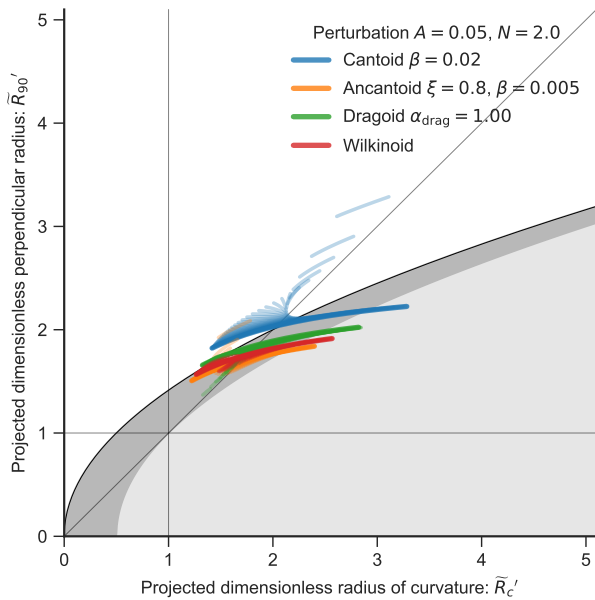


Figure 18. Plane-of-sky projections of perturbed bow shapes. In all cases, the base bow shape is ancantoid with $\xi = 0.8$, $\beta = 0.005$ and the perturbation is the same as in the central panel of Fig. 17, with amplitude $A = 0.05$ and wave number $N = 2.0$. Results are shown for inclination angles $i = 0$ to $i = 75^\circ$ (indicated by line color and thickness, see key) and for different fractional phases of the oscillation: (a) $\varphi = 0.0$, (b) $\varphi = 0.25$, (c) $\varphi = 0.50$. Unlike in Fig. 17, the spatial coordinates are normalized to the instantaneous projected apex radius R'_0 at each phase, so the apex does not appear to move.

**Figure A1.** Divergent dragoids**Figure 19.** Diagnostic diagram for perturbed shapes